The Astrophysical Journal, 870:24 (6pp), 2019 January 1 https://doi.org/10.3847/1538-4357/aaef7e

A Hyperfine-resolved Rotation–Vibration Line List of Ammonia (NH_3)

Phillip A. Coles[1], Alec Owens[2,3], Jochen Küpper[2,3,4], and Andrey Yachmenev[2,3,5]
[1] Department of Physics and Astronomy, University College London, Gower Street, London WC1E 6BT, UK
[2] Center for Free-Electron Laser Science, Deutsches Elektronen-Synchrotron DESY, Notkestrasse 85, D-22607 Hamburg, Germany; andrey.yachmenev@cfel.de
[3] The Hamburg Center for Ultrafast Imaging, Universität Hamburg, Luruper Chaussee 149, D-22761 Hamburg, Germany
[4] Department of Physics, Universität Hamburg, Luruper Chaussee 149, D-22761 Hamburg, Germany
Received 2018 September 14; revised 2018 November 5; accepted 2018 November 6; published 2018 December 31

Abstract

A comprehensive, hyperfine-resolved rotation–vibration line list for the ammonia molecule ($^{14}NH_3$) is presented. The line list, which considers hyperfine nuclear quadrupole coupling effects, has been computed using robust, first principles methodologies based on a highly accurate empirically refined potential energy surface. Transitions between levels with energies below 8000 cm^{-1} and total angular momentum $F \leqslant 14$ are considered. The line list shows excellent agreement with a range of experimental data and will significantly assist future high-resolution measurements of NH_3, both astronomically and in the laboratory.

Key words: astronomical databases: miscellaneous – infrared: general – molecular data

1. Introduction

Ammonia (NH_3) has been detected in a wide variety of astrophysical environments and is an excellent molecular tracer because of its hyperfine structure. In local thermodynamic equilibrium (LTE) conditions, the relative line strengths of the hyperfine components provide a convenient way of deducing the optical depth (Mangum & Shirley 2015), and subsequently characterizing the physical properties of molecular clouds (Ho & Townes 1983). This approach avoids any of the complications associated with isotopologue comparisons, such as the assumption that one knows the isotopologue ratio, and there is no fractionation between the atomic ratio and molecular ratio. Anomalies between the observed and theoretically predicted hyperfine spectra are frequently observed in stellar cores, and while usually attributed to non-LTE conditions (-Matsakis et al. 1977; Stutzki & Winnewisser 1985) or systematic infall/outflow (Park 2001), are still not well understood (Camarata et al. 2015). Accounting for hyperfine effects in spectroscopic observations is thus highly desirable and a detailed understanding of the underlying hyperfine patterns of rotation–vibration energy levels (Twagirayezu et al. 2016) can even benefit the interpretation of spectra measured with Doppler-limited resolution.

The hyperfine structure of the rovibrational energy levels is often described using effective Hamiltonian models (Hougen 1972; Gordy & Cook 1984), albeit even at 100 Hz precision (van Veldhoven et al. 2004), but the limited amount of hyperfine-resolved spectroscopic data means that these models become unreliable when extrapolating to spectral regions not sampled by the experimental data. More successful in their predictive power over extended frequency ranges are variational approaches, which intrinsically treat all resonant interactions between the rovibrational states. Such calculations are becoming increasingly useful in astronomical applications (Tennyson & Yurchenko 2012; Tennyson et al. 2016). For example, variationally computed molecular line lists for methane (Yurchenko & Tennyson 2014) and ammonia (Yurchenko et al. 2011a) were used to assign lines in the near-infrared spectra of late T dwarfs (Canty et al. 2015).

[5] https://www.controlled-molecule-imaging.org

Recently, a generalized variational method for computing the nuclear quadrupole hyperfine effects in the rovibrational spectra of polyatomic molecules was reported by two of the authors (Yachmenev & Küpper 2017). Utilizing this approach, we present a newly computed, hyperfine-resolved rotation–vibration line list for $^{14}NH_3$, applicable for high-resolution measurements in the microwave and near-infrared. Despite a reasonable amount of experimental and theoretical data on the quadrupole hyperfine structure of NH_3 having been reported in the literature, (see Kukolich 1967; Dietiker et al. 2015; and Augustovičová et al. 2016, and references therein), we are aware of only two extensive, hyperfine-resolved line lists (Coudert & Roueff 2006; Yachmenev & Küpper 2017). The work presented here is an improvement on both of these efforts and should greatly facilitate future measurements of NH_3, both astronomically and in the laboratory.

The paper is structured as follows. The line list calculations are described in Section 2, including details on the potential energy surface (PES), dipole moment surface (DMS), electric field gradient (EFG) tensor surface, and variational nuclear motion computations. In Section 3, the line list is presented along with comparisons against a range of experimental data. Concluding remarks are offered in Section 4.

2. Line List Calculations

Variational calculations employed the computer program TROVE (Yurchenko et al. 2007, 2017; Yachmenev & Yurchenko 2015) in conjunction with a recent implementation to treat hyperfine effects at the level of the nuclear quadrupole coupling (Yachmenev & Küpper 2017), which is described by the interaction of the nuclear quadrupole moments with the EFG at the nuclei. Since the methodology of TROVE is well documented and hyperfine-resolved calculations on the rovibrational spectrum of NH_3 have been described (Yachmenev & Küpper 2017), we summarize only the key details relevant for this work.

Initially, the spin-free rovibrational problem was solved for NH_3 to obtain the energies and wavefunctions for states up to $J = 14$, where J is the rotational angular momentum quantum number. The computational procedure for this stage is described in Yurchenko et al. (2011a), however, in this work

we have used a new, highly accurate, empirically refined PES (Coles et al. 2018b). For solving the pure vibrational ($J = 0$) problem, the size of the primitive vibrational basis set was truncated with the polyad number $P_{\max} = 34$. The resulting basis of vibrational wavefunctions was then contracted to include states with energies up to $hc \cdot 20\,000\ \mathrm{cm}^{-1}$ (h is the Planck constant and c is the speed of light) relative to the zero-point energy. Multiplication with symmetry-adapted symmetric-top wavefunctions produced the final spin-free basis set for solving the $J > 0$ rovibrational problem. The final rovibrational wavefunctions, combined with the nuclear spin functions, were used as a basis for solving the eigenvalue problem for the total spin-rovibrational Hamiltonian. The latter is composed of a sum of the diagonal representation of the pure rovibrational Hamiltonian and the non-diagonal matrix representation of the quadrupole coupling. The spin-rovibrational Hamiltonian is diagonal in F, the quantum number of the total angular momentum operator $\boldsymbol{F} = \boldsymbol{J} + \boldsymbol{I}_{\mathrm{N}}$, which is the sum of the rovibrational $\boldsymbol{J}$ and the nuclear spin $\boldsymbol{I}_{\mathrm{N}}$ angular momentum operators.

Besides a PES, calculations require a dipole moment surface (DMS) for the computation of line strengths, and an EFG tensor surface. The ab initio EFG tensor surface at the quadrupolar nucleus ^{14}N was generated on a grid of 4700 symmetry-independent molecular geometries of NH_3 using the coupled cluster method, CCSD(T), with all electrons correlated in conjunction with the augmented correlation-consistent core-valence basis set, aug-cc-pwCVQZ (Dunning 1989; Kendall et al. 1992; Peterson & Dunning 2002). Calculations utilized analytical coupled cluster energy derivatives (Scuseria 1991) as implemented in the CFOUR program package.[6] The elements of the EFG tensor were converted into a symmetry-adapted form in the $\boldsymbol{D}_{3\mathrm{h}}$(M) molecular symmetry group and represented by symmetry-adapted power series expansions up to sixth-order. Details on the representation and least-squares fitting procedure can be found in Yachmenev & Küpper (2017). Similarly, the ab initio DMS was calculated at the CCSD(T)/aug-cc-pCVQZ level of theory with all electrons correlated on the same grid of nuclear geometries as the EFG tensor. The least-squares fitting by analytical expansions was performed following the method described in Yurchenko et al. (2009) and Owens & Yachmenev (2018). A value of $eQ = 20.44$ mb for the ^{14}N nuclear quadrupole constant was used in calculations (Pyykkö 2008). The optimized parameters of the EFG tensor surface, along with the Fortran 90 functions to construct it, are provided as supplementary material (Coles et al. 2018a).

The computed hyperfine-resolved rovibrational line list for $^{14}NH_3$ corresponds to wavelengths $\lambda > 1.25\ \mu$m and considers all transitions between states with energy $E \leqslant hc \cdot 8000\ \mathrm{cm}^{-1}$ relative to the zero-point level and $F \leqslant 14$, where $F = |J - I_{\mathrm{N}}|, \ldots, J + I_{\mathrm{N}}$ and $I_{\mathrm{N}} = 1$. The format of the line list includes information on the initial and final rovibrational states involved in each transition, such as its wavenumber in cm^{-1}, symmetry, and quantum numbers. The line list is provided as supplementary material (Coles et al. 2018a), along with programs to extract user-desired transition data.

3. Results

In Figure 1, and Tables 1 and 2, the predicted quadrupole hyperfine transition frequencies and intensities for NH_3 are compared with the available experimental data for the rotational transitions in the ground vibrational (Coudert & Roueff 2006) and ν_2 (Belov et al. 1998) states, and rovibrational transitions from the ground to the ν_1, $\nu_3^{\pm1}$, $2\nu_4^0$, and $2\nu_4^{\pm2}$ vibrational states (Dietiker et al. 2015). A detailed survey of the available experimental and theoretical data for the quadrupole hyperfine structure of NH_3 can be found in Dietiker et al. (2015) and Augustovičová et al. (2016).

The absolute errors in the rovibrational frequencies are within the accuracy of the underlying PES (Coles et al. 2018b) and are reflective of what is achievable with variational nuclear motion calculations, i.e., sub-cm^{-1} or better. To estimate the accuracy of the predicted quadrupole splittings and the underlying EFG surface, we have subtracted the respective error in the rovibrational frequency unperturbed from the quadrupole interaction effect for each transition. The resulting errors range from 0.1 to 46 kHz for the ground vibrational state (Figure 1) and from 1 to 64 kHz for the ν_2 state (Table 1). Two lines in Table 1 have inconsistently large deviations of 379 and 147 kHz from experiments, that do not correlate with the systematic errors of the calculation. Notably, these lines have the largest experimental uncertainties (of 500 kHz) and may not have been well resolved in experiments due to broadening by spin–spin interactions. The root-mean-square errors for the ground vibrational and ν_2 states are 9 kHz and 72 kHz, or 20 kHz if neglecting the two lines with irregular deviations, respectively. For other fundamental and overtone bands listed in Table 2, the discrepancies are larger by up to 160 kHz; however, the estimated uncertainty of the experimental data is $\pm$100 kHz (Dietiker et al. 2015), giving us confidence that the errors in our predictions are reasonably consistent. Due to the limited amount of available experimental data with hyperfine-resolved structure, it has not been possible to determine reliable systematic errors in our computed quadrupole splittings, particularly with regard to increasing J and k quanta.

Since quadrupole patterns are distinctive to a given rotational transition, they can be very useful for validating spectroscopic assignments. Therefore, the precision of the predicted quadrupole patterns is a good gauge of the line list accuracy. In Table 1 and Table 2 we have evaluated the accuracy of the quadrupole patterns using the expression $\frac{1}{2}\left(\frac{\Delta_{\mathrm{calc}}}{\Delta_{\mathrm{obs}}} - \frac{\Delta_{\mathrm{obs}}}{\Delta_{\mathrm{calc}}}\right)$ (Tashkun et al. 2015), where Δ_{calc} and Δ_{obs} are the calculated and the observed quadrupole line positions relative to the line with maximal calculated intensity within each rovibrational band of quadrupole lines. The numbers are listed only for the quadrupole splittings that are larger than the estimated experimental uncertainty. The calculated quadrupole patterns reproduce the experiments very well, with most discrepancies within a few percent. There is a notable correlation between larger discrepancies and larger ratios between the experimental uncertainty and relative quadrupole line position. The largest pattern accuracy value of 120.89% occurs in the ν_1 band, but this value is inconsistent with the values for the other transitions, hinting at a possibly larger experimental uncertainty for this transition. Overall, the agreement of the presented line list with experiments has improved in comparison to the previous theoretical study (Yachmenev & Küpper 2017), which was based on an older PES (Yurchenko et al. 2011b) and an EFG tensor computed with a lower level of ab initio theory.

[6] For the current version, see http://www.cfour.de/.

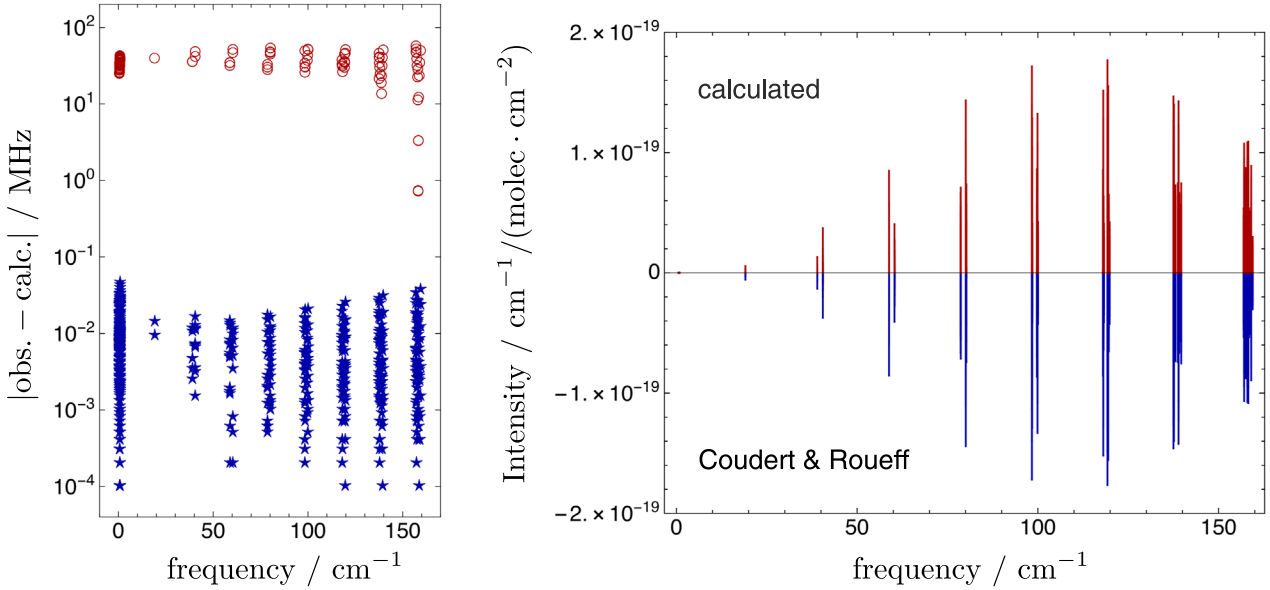

Figure 1. Discrepancies of the calculated transition frequencies of NH_3 relative to the experimental data for the ground ν_0 vibrational state (left panel; Coudert & Roueff 2006) together with the calculated and observed spectrum (right panel). The errors in the rovibrational frequencies are plotted with red circles, while the relative errors of the quadrupole splittings are plotted with blue stars.

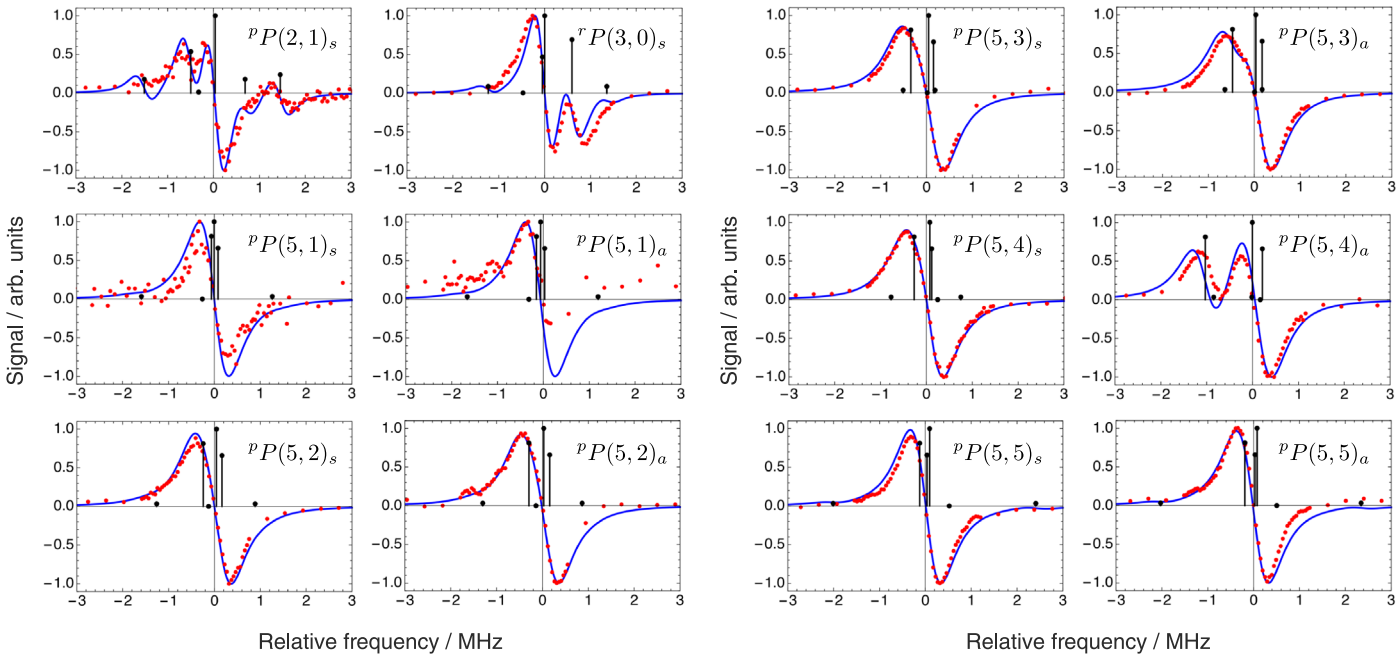

Figure 2. Comparison of the calculated (blue line) and observed (red dots; Twagirayezu et al. 2016) saturation dip line shapes for the ${}^{\Delta K_a}\Delta J(J'', K_a'')_{\tau_{\rm inv}''}$ transitions of the $\nu_1+\nu_3$ band of NH_3 ($\tau_{\rm inv}'' = s$ or a denotes *symmetric* or *anti-symmetric* inversion parity of the ground vibrational state, and $''$ denotes the lower state). The black stems depict the calculated stick spectrum. The experimental and calculated intensities are normalized to the respective maximal values. The measured (calculated) zero-crossing wavenumbers, in cm^{-1}, are 6572.85349 (6572.81120) for ${}^pP(2, 1)_s$, 6544.32154 (6544.28589) for ${}^rP(3, 0)_s$, 6513.77250 (6513.73344) for ${}^pP(5, 1)_s$, 6513.65575 (6513.59558) for ${}^pP(5, 1)_a$, 6521.97101 (6521.93627) for ${}^pP(5, 2)_s$, 6522.23374 (6522.25564) for ${}^pP(5, 2)_a$, 6529.18969 (6529.18151) for ${}^pP(5, 3)_s$, 6528.76857 (6528.74384) for ${}^pP(5, 3)_a$, 6536.59280 (6536.55360) for ${}^pP(5, 4)_s$, 6537.68063 (6538.22791) for ${}^pP(5, 4)_a$, 6542.62402 (6542.63130) for ${}^pP(5, 5)_s$, and 6542.42400 (6542.44221) for ${}^pP(5, 5)_a$.

Figure 2 shows comparisons with the sub-Doppler saturation dip spectroscopic measurements for the $\nu_1 + \nu_3$ band of NH_3 (Twagirayezu et al. 2016; T. J. Sears 2017, private communication). The saturation dip line shapes were calculated as the intensity-weighted sums of Lorentzian line-shape derivatives (Axner et al. 2001) with a half-width-at-half-maximum (HWHM) of the absorption profile of 290 kHz and a HWHM-amplitude of the experimentally applied frequency-modulation dither of 150 kHz (T. J. Sears 2017, private communication). A slightly larger HWHM

Table 1
Discrepancies of the Calculated Transition Frequencies (Obs−Calc) and Intensities (I) with Respect to the Experimental Data for the ν_2 Vibrational State of NH_3 (Belov et al. 1998)

J'	k'	τ'_{inv}[a]	F'	J''	k''	τ''_{inv}	F''	Obs (MHz)[b]	Obs−Calc (MHz)		Relative I		Absolute I[c]	Pattern Accuracy (%)[d]
									Absolute	Relative	Obs	Calc		
1	1	a	1	2	1	s	2	140140.794(060)	606.842	−0.014	90.00	90.00	7.532×10^{-25}	−1.04
1	1	a	1	2	1	s	1	140141.902(250)	606.854	−0.003	30.00	30.00	2.511×10^{-25}	−1.22
1	1	a	2	2	1	s	1	140142.163(500)	606.478	−0.379	2.00	1.96	1.637×10^{-26}	⋯
1	1	a	2	2	1	s	3	140142.150(025)	606.856	0.000	168.00	168.00	1.406×10^{-24}	*
1	1	a	2	2	1	s	2	140141.427(060)	606.838	−0.018	30.00	30.00	2.511×10^{-25}	−2.52
1	1	a	0	2	1	s	1	140143.503(030)	606.862	0.006	40.00	40.00	3.348×10^{-25}	−0.44
2	2	a	1	3	2	s	2	741789.155(002)	595.343	0.000	252.00	252.00	1.574×10^{-23}	−0.03
2	2	a	3	3	2	s	4	741788.397(006)	595.343	0.000	540.00[e]	540.00	3.372×10^{-23}	*
2	2	a	3	3	2	s	3	741788.399(050)	595.344	0.001	46.67	46.67	2.914×10^{-24}	⋯
2	2	a	3	3	2	s	2	741788.403(100)	595.349	0.006	1.33	1.18	7.395×10^{-26}	⋯
2	2	a	3	3	2	s	4	741788.398(005)[f]	595.344	0.001	540.00[e]	540.00	3.372×10^{-23}	⋯
2	2	a	3	3	2	s	3	741788.388(050)[f]	595.333	−0.010	46.67	46.67	2.914×10^{-24}	⋯
2	2	a	3	3	2	s	2	741788.355(050)[f]	595.301	−0.042	1.33	1.18	7.395×10^{-26}	⋯
2	2	a	2	3	2	s	3	741787.015(005)	595.324	−0.018	373.33	373.33	2.331×10^{-23}	−1.31
2	2	a	2	3	2	s	2	741787.020(050)	595.330	−0.012	46.67	46.67	2.914×10^{-24}	−0.88
2	2	a	2	3	2	s	3	741787.019(010)[f]	595.328	−0.014	373.33	373.33	2.331×10^{-23}	−1.02
2	2	a	2	3	2	s	2	741786.987(050)[f]	595.297	−0.045	46.67	46.67	2.914×10^{-24}	−3.24
2	0	a	3	3	0	s	4	769710.287(015)	576.907	0.000	540.00[e]	540.00	1.199×10^{-22}	*
2	0	a	2	3	0	s	3	769710.281(035)	576.932	0.026	373.33	373.35	8.291×10^{-23}	⋯
2	0	a	3	3	0	s	4	769710.289(015)[f]	576.909	0.002	540.00[e]	540.00	1.199×10^{-22}	⋯
2	0	a	2	3	0	s	3	769710.277(025)[f]	576.928	0.022	373.33	373.35	8.291×10^{-23}	⋯
2	0	a	1	3	0	s	2	769710.000(010)	576.890	−0.017	252.00	252.00	5.596×10^{-23}	−6.11
2	0	a	3	3	0	s	3	769708.896(020)	576.915	0.009	46.67	46.67	1.036×10^{-23}	0.64
2	0	a	3	3	0	s	2	769710.630(500)	576.760	−0.147	1.33	1.18	2.618×10^{-25}	⋯
2	0	a	2	3	0	s	2	769712.123(015)	576.885	−0.022	46.67	46.67	1.036×10^{-23}	1.19
2	1	a	3	3	1	s	3	762851.494(020)	590.129	−0.037	46.67	21.78	4.685×10^{-24}	−3.33
2	1	a	3	3	1	s	4	762852.624(025)	590.166	0.000	252.00	252.00	5.421×10^{-23}	*
2	1	a	1	3	1	s	2	762852.624(030)	590.163	−0.003	540.00[e]	117.60	2.530×10^{-23}	⋯
2	1	a	3	3	1	s	2	762852.942(050)	590.102	−0.064	1.33	0.55	1.185×10^{-25}	18.44
2	1	a	2	3	1	s	3	762852.209(005)	590.160	−0.006	373.33	174.22	3.748×10^{-23}	−1.46
2	1	a	2	3	1	s	2	762853.684(005)	590.160	−0.006	46.67	21.78	4.685×10^{-24}	0.56
1	0	s	0	0	0	a	1	466243.620(002)	−610.769	−0.007	4.00	4.31	5.656×10^{-24}	−0.35
1	0	s	2	0	0	a	1	466245.605(005)	−610.762	0.000	20.00	20.00	2.625×10^{-23}	*
1	0	s	1	0	0	a	1	466246.945(003)	−610.740	0.022	12.00	12.93	1.697×10^{-23}	−1.66

Notes. The relative errors (obs−calc/relative) are computed as quadrupole shifts with respect to the line, with maximal intensity for each rovibrational band, i.e., lines with the same J'', k'', τ''_{inv} and J', k', τ'_{inv}, but different F'' and F'. The calculated relative intensities (relative I/calc) are obtained by scaling to the maximal observed relative intensity (relative I/obs) within each rovibrational band of quadrupole-split Lines.

[a] $\tau_{inv} = s$ or a denotes *symmetric* or *anti-symmetric* inversion parity of the ν_2 vibrational state.

[b] Experimental uncertainties in parentheses are in the units of the last reported digits; see Table 1 in Belov et al. (1998).

[c] The calculated absolute intensities for $T = 300$ K are in units of $cm^{-1}/(molecule\ cm^{-2})$.

[d] $\frac{1}{2}\left(\frac{\Delta_{calc}}{\Delta_{obs}} - \frac{\Delta_{obs}}{\Delta_{calc}}\right)$, where Δ_{calc} and Δ_{obs} are the calculated and the observed quadrupole-split line positions relative to the line with maximal calculated intensity (marked with asterisks) within each rovibrational band of quadrupole-split lines. The pattern accuracy factors are listed only for the quadrupole splittings that are larger than the estimated experimental uncertainty.

[e] Largest observed value; see Belov et al. (1998).

[f] Semi-experimental frequencies obtained using the crossover peak frequencies; see Belov et al. (1998).

was employed for the measured ${}^pP(5, K''_a)$ transitions (T. J. Sears 2017, private communication) and we have found a value of 500 kHz reproduces these line shapes well. Overall, the computed saturation dip profiles are in excellent agreement with experiments. Notably, in our previous theoretical study (Yachmenev & Küpper 2017) we could not explain the observed double-peak feature of the ${}^pP(5, 4)_a$ transition and instead predicted a double-peak structure in the ${}^pP(5, 3)_a$ transition not seen in the experimental profile. This has now been rectified due to the use of a much improved and more reliable PES (Coles et al. 2018b) and the consideration of core-valence electron correlation in the calculation of the EFG tensor surface. Interestingly, the observed splitting in the ${}^pP(5, 4)_a$ transition at 6777.63638 cm^{-1} arises because the upper state is in fact a superposition of the three states $|J, k, \tau\rangle = |4, 2, 0\rangle$ of $\nu_3 + \nu_4 + 2\nu_2$, $|4, 3, 1\rangle$ of $(\nu_1 + \nu_3)^-$, and $|4, 3, 0\rangle$ of $(\nu_1 + \nu_3)^-$, with approximately equal squared-coefficient contributions, where τ reflects the rotational parity defined as $(-1)^\tau$.

Table 2
Discrepancies of the Calculated Transition Frequencies (Obs−Calc) with Respect to the Experimental Data for the ν_1, $\nu_3^{\pm1}$, $2\nu_4^0$, $2\nu_4^{\pm2}$ Bands of NH_3 (Dietiker et al. 2015)

Vibr. Level	J'	k'	$\tau'_{\rm inv}$ [a]	F'	J''	k''	$\tau''_{\rm inv}$	F''	Obs (MHz)	Obs−Calc (MHz)		Intensity[b]	Pattern Accuracy (%)[c]
										Absolute	Relative		
ν_1	1	1	a	1	2	1	s	2	101166502.618	−115.842	−0.009	1.228×10^{-21}	−0.72
	1	1	a	2	2	1	s	2	101166503.217	−115.850	−0.016	4.094×10^{-22}	−2.45
	1	1	a	1	2	1	s	1	101166503.787	−115.673	0.160	4.094×10^{-22}	120.89
	1	1	a	2	2	1	s	3	101166503.877	−115.833	0.000	2.292×10^{-21}	*
	1	1	a	0	2	1	s	1	101166505.196	−115.782	0.051	5.458×10^{-22}	−3.94
	0	0	a	1	1	0	s	1	100580586.109	−76.131	−0.029	2.249×10^{-21}	−2.39
	0	0	a	1	1	0	s	2	100580587.338	−76.102	0.000	3.748×10^{-21}	*
	0	0	a	1	1	0	s	0	100580589.137	−76.103	−0.001	7.704×10^{-29}	0.06
$\nu_3^{\pm1}$	0	0	a	1	1	1	a	0	103686651.285	−279.126	−0.136	2.231×10^{-29}	−13.51
	0	0	a	1	1	1	a	2	103686652.364	−278.989	0.000	1.784×10^{-21}	*
	0	0	a	1	1	1	a	1	103686652.874	−279.109	−0.119	1.070×10^{-21}	21.13
$2\nu_4^0$	0	0	a	1	1	0	s	1	97010274.474	148.905	0.164	1.609×10^{-22}	14.56
	0	0	a	1	1	0	s	0	97010277.532	148.929	0.188	9.758×10^{-30}	−9.85
	0	0	a	1	1	0	s	2	97010275.524	148.741	0.000	2.681×10^{-22}	*
$2\nu_4^{\pm2}$	0	0	a	1	1	1	a	0	97485902.014	670.652	−0.021	1.194×10^{-29}	−2.28
	0	0	a	1	1	1	a	2	97485902.944	670.672	0.000	3.540×10^{-22}	*
	0	0	a	1	1	1	a	1	97485903.543	670.666	−0.006	2.124×10^{-22}	1.00

Notes. The relative errors (obs−calc/relative) are computed as quadrupole shifts with respect to the line with maximal intensity for each rovibrational band of quadrupole-split transitions, i.e., lines with the same J'', k'', $\tau''_{\rm inv}$, and J', k', $\tau'_{\rm inv}$, but different F'' and F'.

[a] $\tau_{\rm inv} = s$ or a denotes the *symmetric* or *anti-symmetric* inversion parity of the vibrational state.

[b] The calculated absolute intensities for $T = 300$ K are in units of $\rm cm^{-1}/(molecule\ cm^{-2})$.

[c] $\frac{1}{2}\left(\frac{\Delta_{\rm calc}}{\Delta_{\rm obs}} - \frac{\Delta_{\rm obs}}{\Delta_{\rm calc}}\right)$, where $\Delta_{\rm calc}$ and $\Delta_{\rm obs}$ are the calculated and the observed quadrupole-split line positions relative to the line with maximal calculated intensity (marked with asterisks) within each rovibrational band of quadrupole-split lines.

4. Conclusions

A new rotation–vibration line list for $^{14}NH_3$, which accounts for nuclear quadrupole hyperfine effects, has been presented. Comparisons with a range of experimental results showed excellent agreement, validating the computational approach that was taken. Notably, the new line list allowed us to resolve line-shape discrepancies when compared with a previous hyperfine-resolved line list computed by two of the authors (Yachmenev & Küpper 2017). Due to the variational approach that was taken, such improvements can be expected across the 0–8000 $\rm cm^{-1}$ region and can be attributed to the use of a highly accurate empirically refined PES and more rigorous electronic structure calculations for the EFG tensor surface. The line list contains detailed information, e. g., symmetry and quantum number labeling, for each transition, which will be extremely useful for future analyses of hyperfine-resolved ammonia spectra. Natural extensions to our calculations would be the consideration of a larger wavenumber range and higher energy level threshold; however, work in this direction will only be undertaken if there is a demand for such data.

The spectrum of ammonia is also of interest regarding a possible temporal or spatial variation of the proton–electron mass ratio μ (van Veldhoven et al. 2004). If any such variation has occurred, it would manifest as tiny but observable shifts in the frequencies of certain transitions. Constraints on a varying μ have been deduced using NH_3 in our Galaxy (Levshakov et al. 2010) in objects at high-redshift, e.g., the system B0218 + 357 at redshift $z \sim 0.685$ (Flambaum & Kozlov 2007; Murphy et al. 2008; Kanekar 2011) and PKS1830−211 at $z \sim 0.886$ (Henkel et al. 2009), and are possible in high-precision laboratory setups (van Veldhoven et al. 2004; Cheng et al. 2016). Studying the mass sensitivity (Owens et al. 2015, 2016) of the hyperfine transitions could reveal promising spectral regions to guide future measurements of ammonia, ultimately leading to tighter constraints on drifting fundamental constants.

We gratefully acknowledge Trevor Sears for providing us with their original experimental data. This work has been supported by the *Deutsche Forschungsgemeinschaft* (DFG) through the excellence cluster "The Hamburg Center for Ultrafast Imaging—Structure, Dynamics and Control of Matter at the Atomic Scale" (CUI, EXC1074), by the Helmholtz Association "Initiative and Networking Fund", and by the COST action MOLIM (CM1405). A.O. gratefully acknowledges a fellowship from the Alexander von Humboldt Foundation.

Software: TROVE (Yurchenko et al. 2007; Yachmenev & Yurchenko 2015; Yurchenko et al. 2017), CFOUR (http://www.cfour.de/).

ORCID iDs

Alec Owens https://orcid.org/0000-0002-5167-983X
Jochen Küpper https://orcid.org/0000-0003-4395-9345
Andrey Yachmenev https://orcid.org/0000-0001-8770-6919

References

Augustovičová, L., Soldán, P., & Špirko, V. 2016, ApJ, 824, 147
Axner, O., Kluczynski, P., & Lindberg, M. 2001, JQRST, 68, 299

Belov, S., Urban, Š., & Winnewisser, G. 1998, JMoSp, 189, 1
Camarata, M. A., Jackson, J. M., & Chambers, E. 2015, ApJ, 806, 74
Canty, J. I., Lucas, P. W., Yurchenko, S. N., et al. 2015, MNRAS, 450, 454
Cheng, C., van der Poel, A. P. P., Jansen, P., et al. 2016, PhRvL, 117, 253201
Coles, P., Owens, A., Küpper, J., & Yachmenev, A. 2018a, Supplementary material: Hyperfine-resolved Rotation-vibration Line List of Ammonia (NH_3), Zenodo, doi:10.5281/zenodo.1414346
Coles, P. A., Ovsyannikov, R. I., Polyansky, O. L., Yurchenko, S. N., & Tennyson, J. 2018b, JQSRT, 219, 199
Coudert, L. H., & Roueff, E. 2006, A&A, 449, 855
Dietiker, P., Miloglyadov, E., Quack, M., Schneider, A., & Seyfang, G. 2015, JChPh, 143, 244305
Dunning, T. H. 1989, JChPh, 90, 1007
Flambaum, V. V., & Kozlov, M. G. 2007, PhRvL, 98, 240801
Gordy, W., & Cook, R. L. 1984, Microwave Molecular Spectra (3rd ed.; New York: Wiley)
Henkel, C., Menten, K. M., Murphy, M. T., et al. 2009, A&A, 500, 725
Ho, P. T. P., & Townes, C. H. 1983, ARA&A, 21, 239
Hougen, J. T. 1972, JChPh, 57, 4207
Kanekar, N. 2011, ApJL, 728, L12
Kendall, R. A., Dunning, T. H., Jr., & Harrison, R. J. 1992, JChPh, 96, 6796
Kukolich, S. G. 1967, PhRv, 156, 83
Levshakov, S. A., Lapinov, A. V., Henkel, C., et al. 2010, A&A, 524, A32
Mangum, J. G., & Shirley, Y. L. 2015, PASP, 127, 266
Matsakis, D. N., Brandshaft, D., Chui, M. F., et al. 1977, ApJL, 214, L67
Murphy, M. T., Flambaum, V. V., Muller, S., & Henkel, C. 2008, Sci, 320, 1611
Owens, A., & Yachmenev, A. 2018, JChPh, 148, 124102
Owens, A., Yurchenko, S. N., Thiel, W., & Špirko, V. 2015, MNRAS, 450, 3191
Owens, A., Yurchenko, S. N., Thiel, W., & Špirko, V. 2016, PhRvA, 93, 052506
Park, Y.-S. 2001, A&A, 376, 348
Peterson, K. A., & Dunning, T. H. 2002, JChPh, 117, 10548
Pyykkö, P. 2008, MolPh, 106, 1965
Scuseria, G. E. 1991, JChPh, 94, 442
Stutzki, J., & Winnewisser, G. 1985, A&A, 144, 13
Tashkun, S., Perevalov, V., Gamache, R., & Lamouroux, J. 2015, JQSRT, 152, 45
Tennyson, J., & Yurchenko, S. N. 2012, MNRAS, 425, 21
Tennyson, J., Yurchenko, S. N., Al-Refaie, A. F., et al. 2016, JMoSp, 327, 73
Twagirayezu, S., Hall, G. E., & Sears, T. J. 2016, JChPh, 145, 144302
van Veldhoven, J., Küpper, J., Bethlem, H. L., et al. 2004, EPJD, 31, 337
Yachmenev, A., & Küpper, J. 2017, JChPh, 147, 141101
Yachmenev, A., & Yurchenko, S. N. 2015, JChPh, 143, 014105
Yurchenko, S. N., Barber, R. J., & Tennyson, J. 2011a, MNRAS, 413, 1828
Yurchenko, S. N., Barber, R. J., Tennyson, J., Thiel, W., & Jensen, P. 2011b, JMoSp, 268, 123
Yurchenko, S. N., Barber, R. J., Yachmenev, A., et al. 2009, JPCA, 113, 11845
Yurchenko, S. N., & Tennyson, J. 2014, MNRAS, 440, 1649
Yurchenko, S. N., Thiel, W., & Jensen, P. 2007, JMoSp, 245, 126
Yurchenko, S. N., Yachmenev, A., & Ovsyannikov, R. I. 2017, J. Chem. Theory Comput., 13, 4368